Radiation-induced micro-structures as ground states of a Swift-Hohenberg energy functional

David Simeone, G J Thorogood, G L Murphy, A Forestier, P Garcia, L Luneville

Journal of Applied Physics

Radiation-induced micro-structures as ground states of a Swift-Hohenberg energy functional

Cite as: J. Appl. Phys. **125**, 065103 (2019); https://doi.org/10.1063/1.5072798
Submitted: 21 October 2018 . Accepted: 21 January 2019 . Published Online: 08 February 2019

D. Simeone, G. J. Thorogood, G. L. Murphy, A. Forestier, P. Garcia, and L. Luneville

Journal of Applied Physics ARTICLE scitation.org/journal/jap

Radiation-induced micro-structures as ground states of a Swift-Hohenberg energy functional

Cite as: J. Appl. Phys. **125**, 065103 (2019); doi: 10.1063/1.5072798
Submitted: 21 October 2018 · Accepted: 21 January 2019 ·
Published Online: 8 February 2019

D. Simeone,[1,2] G. J. Thorogood,[3,4] G. L. Murphy,[3,5] A. Forestier,[6] P. Garcia,[7] and L. Luneville[2,8]

AFFILIATIONS

[1]CEA/DEN/DMN/SRMA/LA2M-LRC CARMEN, CEA, Université Paris-Saclay, F-91191 Gif-sur-Yvette, France
[2]CNRS/ECP/UMR 8085, Grande voie des vignes, Chatenay Malabry, France
[3]ANSTO, Lucas Heights, New South Wales, Australia
[4]Department of Nuclear System Safety Engineering, Nagaoka University of Technology, 1603-1 Kamitomioka, Nagaoka 940-2188, Japan
[5]Department of Nuclear System Safety Engineering, School of Chemistry, The University of Sydney, Sydney, New South Wales 2006, Australia
[6]CEA/DEN/DANS, Université Paris-Saclay, F-91191 Gif-sur-Yvette, France
[7]CEA, DEN, DEC, Centre de Cadarache, 13108 Saint-Paul-Lez-Durance Cedex, France
[8]CEA/DEN/DM2S/SERMA/LLPR-LRC CARMEN, CEA, Université Paris-Saclay, F-91191 Gif-sur-Yvette, France

ABSTRACT

We demonstrate that the Swift-Hohenberg functional, which is used to describe patterning observed in out of equilibrium systems such as diblock copolymers, Rayleigh-Benard convection, and thin film magnetic garnets, can be applied to radiation-induced patterns that occur in non-miscible alloys. By comparing ground states obtained from the minimization of this functional and a 2D numerical simulation performed on an irradiated AgCu material, which is the archetype of a non-miscible alloy, we show that the Swift-Hohenberg functional provides all possible patterns generated under irradiation and the solubility limits of radiation-induced precipitates in these patterns. To rationalize the formation of these radiation-induced patterns, we propose a generic "pseudophase diagram" that relies not only on the irradiation flux and temperature but also on the overall composition of the alloy. Tuning this overall composition offers the opportunity to tailor new materials with various micro-structures overcoming the limitation of the equilibrium phase diagram.

I. INTRODUCTION

Materials ranging from ferro-fluids to polymers, when at equilibrium, can exhibit distinct patterns,[1,2] which can be computed from ground states of their free energy.[2,3] In systems far from equilibrium, such as solids under irradiation or submitted to intense deformation,[4] experimental observations have also revealed the existence of such patterns.[5,6] Experimental irradiation-induced dislocation lattices[7] can be readily modeled via reaction-diffusion type equations within a chemical rate theory framework.[7,8] However, there is presently no overarching theory that predicts and models the patterns resulting from irradiation-induced disordering.

At the atomic scale, molecular dynamics (MD) is used to predict how metals and oxides will behave when exposed to radiation over interatomic distances; its strength lies in the ability to predict the initial stage of radiation damage. It is, however, limited to pico-second ranges. Further along the length and time scale lies Kinetic Monte Carlo (KMC);[9,10] it is capable of describing point defects and dislocations. However, this method is still limited by the size of the simulation box and time.[8] Due to these limitations, attempts have been made to develop modeling of disordering generated by ion beam mixing at larger space and time scales within the phase field framework.[8,11–13]

In this study, we have examined the formation of radiation-induced disordering patterns within the phase field framework, the continuum counterpart of the atomic Ising model extensively used in KMC simulations of disordering.[9,14]

The postulate, commonly admitted in the radiation damage community, is that radiation-induced patterns can emerge from the balance of disordering effects induced by ion beam mixing (hereafter called ballistic effects[8] controlled by the irradiation flux ϕ) and radiation enhanced diffusion processes tuned by the temperature T. This balance leads to the formation of unexpected patterns when compared with those predicted under the thermodynamic equilibrium.[11,15]

This work highlights that the Swift-Hohenberg (SH) functional,[16] extensively used to discuss the formation and the stability of patterns in materials produced out of equilibrium,[2,3] can predict the appearance of all possible ground states (nanostructures) associated with these radiation-induced patterns. This SH functional was extensively used in the Phase Field Crystal (PFC) approach initially devoted to the crystal growth kinetics at the atomic scale.[17–19] The ultimate goal of this work is to show that a SH functional can also be introduced to discuss radiation-induced patterning. Even if the SH functional developed in this work cannot be derived from first principles at the atomic scale such as the PFC, it demonstrates that all tools developed for understanding pattern formations and their stability produced by such a functional can be applied to radiation-induced patterning. The novelty of this study lies in two aspects. First, we illustrate with an example (AgCu non-miscible alloy) that the approximation of the Lyapunov function describing the dynamics of radiation-induced microstructures, with a SH functional, allows one to predict the entire set of patterns that is produced by ion beam mixing. Secondly, we generalize the "dynamical phase diagram" generated under irradiation to include, along with temperature and incident particle flux, the overall composition of the alloy, the effect of which has been overlooked in previous studies.[11,15]

II. CONSTITUTIVE EQUATIONS

Disordering of non-miscible $A_{\bar{c}}B_{1-\bar{c}}$ alloys of overall composition $\bar{c}$ via irradiation is the result of a re-distribution of atomic species via their thermal mobility enhanced by vacancies produced by the ion beam (or neutron flux) $\Gamma_{th}(T, \phi)$[13] and atom relocation, which is triggered by ballistic effects due to atomic collisions in the crystal, $\Gamma_{irr}(\phi)$.[11,15] At the nanoscale, the local composition $c(\mathbf{r}, t)$ of species A in the alloy is described by the scalar order parameter field $\eta(\mathbf{r}, t) = c(\mathbf{r}, t) - c_0$, where c_0 is the atomic fraction of species A at the critical temperature T_0, i.e., the temperature for which the order parameter is null. For AgCu alloys, c_0 is equal to 0.38 and the critical temperature, which fitted the experimental equilibrium phase diagram,[12] is equal to 1200 K.[20]

A. Competing dynamics

At low temperatures ($T \ll T_0$), the thermal evolution of the alloy follows a spinodal decomposition as given by[21]

$$\left.\frac{\partial \eta(\mathbf{r}, t)}{\partial t}\right|_{th} = \Gamma_{th}(T, \phi)\nabla^2 \frac{\delta F[\eta]}{\delta \eta}, \tag{1}$$

where $F[\eta] = \int f[\eta(\mathbf{r}, t)]d\mathbf{r}$ represents the free energy of the system. In this expression, the free energy density, $f[\eta(\mathbf{r}, t)]$, is represented by a Landau fourth order expansion, $\frac{a_2}{2}\eta(\mathbf{r}, t)^2 + \frac{a_3}{3}\eta(\mathbf{r}, t)^3 + \frac{a_4}{4}\eta(\mathbf{r}, t)^4$. The third order term is negative as expected for a decomposition transformation, which is a first order transition.[21,22]

The spatial heterogeneity of $\eta(\mathbf{r}, t)$ is represented by adding to $F[\eta]$ the Ginzburg term, $\int \kappa |\nabla \eta(\mathbf{r}, t)|^2 d\mathbf{r}$, where κ is the energetic cost of interfaces forming between separate domains of different compositions[21] ($\kappa > 0$).

Alternatively, the dynamics of $\eta(\mathbf{r}, t)$ induced by the ballistic effects is non-local and can be modeled via[23,24]

$$\left.\frac{\partial \eta(\mathbf{r}, t)}{\partial t}\right|_{irr} = \Gamma_{irr}(\phi)\left[\int p_{R_p}(\mathbf{r} - \mathbf{r}')\eta(\mathbf{r}', t)d\mathbf{r}' - \eta(\mathbf{r}, t)\right], \tag{2}$$

where $p_{R_p}(\mathbf{r})$ is the probability density of an atom relocating in a displacement cascade, which lasts a few hundreds of picoseconds and R_p is the mean free path of the relocated atom.[11,15] R_p depends on the nature of the incident projectiles, the atomic composition of the target, and slightly of the incident energy for particles with kinetic energies below a few MeV.[25] For instance, R_p is equal to 0.3 nm for AgCu samples irradiated by 1 MeV Kr ions.

Equations (1) and (2) result from a space and time coarse-graining method.[11,24] In the Phase Field framework, the coarse-grained time scale is controlled by the diffusion of atoms (few 10^{-6} s, i.e., 4 orders of magnitude larger than the expansion of a displacement cascade) and the space scale is proportional to κ^{-1}, which is one order of magnitude larger than R_p. The main interest of this approach is to incorporate long range elastic fields induced by precipitates.[21]

B. Steady states

The specific form of Eq. (2) enables the modeling of two dynamics, acting in parallel as expected from the postulate, via a relaxation equation[13,15]

$$\left.\frac{\partial \eta(\mathbf{r}, t)}{\partial t}\right|_{tot} = \Gamma_{th}(T, \phi)\nabla^2 \frac{\partial \mathcal{L}[\eta]}{\partial \eta}. \tag{3}$$

The numerical resolution of Eq. (3) is obtained by applying Neumann conditions at the boundaries (no flux at the boundaries) as displayed in Fig. 2. $\mathcal{L}[\eta] = F[\eta] + \frac{\Gamma_{irr}(\phi)}{2\Gamma_{th}(T, \phi)}G[\eta]$ can be understood as the Lyapunov functional for the full set of dynamics. In this functional, the effect of non-local ballistic effects is described by $G[\eta(\mathbf{r}, t)] = \int\int \eta(\mathbf{r}, t)g(\mathbf{r} - \mathbf{r}')\eta(\mathbf{r}', t)d\mathbf{r}d\mathbf{r}'$ [where $\nabla^2 g = (p_{R_p} - \delta)$]. The dynamics behaves as if it was at $T = 0$ with a temperature dependence only entering through T-dependent model parameters and is only subject to random initial conditions associated with a fully disordered state.[26] The challenge of understanding radiation-induced disordering therefore can be posed as finding the nature of ground states of $\mathcal{L}[\eta]$ under the constraint of conservation of the overall value, $\bar{\eta}$, of the order parameter η.

Introducing a space characteristic length, $l_0 = \sqrt{\frac{|a_2|}{a_4\alpha^2}}$ ($\alpha = \frac{\eta_+ - \eta_-}{2}$; $\eta_\pm$ are the solubility limits of the equilibrium phase diagram), it is convenient to compute the dimensionless form of the Lyapunov functional $\mathcal{L}'[\eta] = \frac{\mathcal{L}[\eta]}{F_0}$ ($F_0 = \frac{\alpha\kappa^{\frac{3}{2}}}{\sqrt{a_4}}$) as a function of the reduced scalar order parameter field $\eta(\mathbf{r}, t) = \frac{c(\mathbf{r}, t) - c_0}{\alpha}$, the enhancement factor $\Delta(\phi, T) = \frac{\Gamma_{irr}(\phi)}{\Gamma_{th}(\phi, T)} \frac{\kappa}{\alpha^4 a_4{}^2 \Omega_{at}}$ (Ω_{at} is the mean atomic volume of the alloy), and the reduced mean free path $R = \frac{R_p}{l_0}$. As $\eta(\mathbf{r}, t)$ is small, a generic "dynamical phase diagram" can be derived from the minimization of the quadratic term of $\mathcal{L}'[\eta] = \frac{1}{2}\int D(k)|\hat{\eta}(\mathbf{k}, t)|^2 d\mathbf{k}$ [where $D(k) = -1 + k^2 + \frac{\Delta R^2}{1+R^2k^2}$ is called the response function[13,21] and $\hat{\eta}(\mathbf{k}, t)$ is the Fourier transform of $\eta(\mathbf{x}, t)$]. This generic "dynamical phase diagram," spanned by R and Δ, exhibits three distinct domains associated with two "limit of phases" $\Delta_{min} = R^{-4}$ (dashed line in Fig. 1) and $\Delta_{max} = \frac{(1+R^2)^2}{4R^4}$ (full line in Fig. 1). At high R values, ballistic effects dominate chemical effects and disordering of the alloy occurs leading to a solid solution (SS). At low R values, the ballistic effects are neglected in comparison with the chemical nature of species forming the alloy and a spinodal decomposition (SD) occurs. In this domain, A-rich precipitates of characteristic size $L(t) \propto t^{\frac{1}{3}}$ coarsen.[27] At low temperatures and large relocation distances (PD area), i.e., for $\Delta_{min} < \Delta < \Delta_{max}$, A-rich precipitates stop to coarsen and exhibit a spatial periodicity $\frac{2\pi}{k_0}$ of a few nanometers leading to the formation of nanodomains. This composition modulation is defined by a non-null wave vector $\mathbf{k_0}$ of the modulus $k_0 = (\sqrt{\Delta} - \sqrt{\Delta_{min}})^{\frac{1}{2}}$. The limit between the disordered (SS) and ordered phases (SD and PD) Δ_{max} is given by $D(k_0) = 0$, in perfect agreement with the previous limit derived from a linear analysis of the growth rate of Eq. (3).[15] The limit between (SD) and (PD) domains Δ_{min}, given by the vanishing of k_0,[11] differs from the previous one calculated assuming an *ad hoc* mixed sin-tanh ansatz.[15]

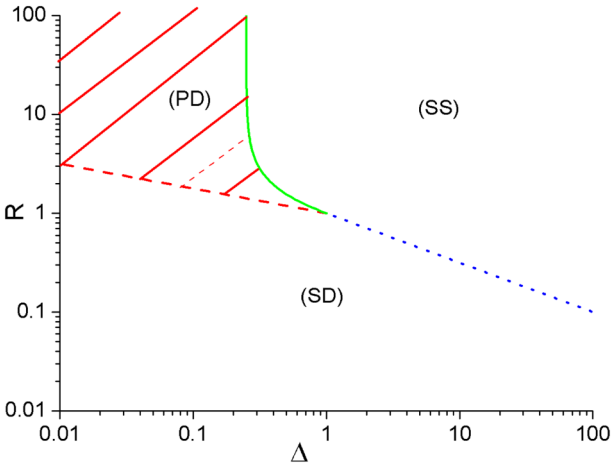

FIG. 1. "Dynamical phase diagram" resulting from the irradiation of non-miscible alloys as a function of the reduced units Δ and *R* irrespective of their overall composition. Three distinct domains can be produced: a disordered domain associated with a solid solution (SS), a domain where the spinodal decomposition (SD) takes place, and a pattern domain (PD) where the coarsening of precipitates is frozen. [dashed red line: limit between the spinodal decomposition and patterning of domains (Δ_{min}), blue dotted line: limit between the (PD) and the (SS)].

III. DERIVATION OF THE SWIFT-HOHENBERG EQUATION

Even if this analysis is sufficient to construct a generic "dynamical phase diagram," information about the possible nano-structures (stripes, droplets, etc.) that emerge in the (PD) area is not revealed. Additionally, as Eq. (3) is a conservative equation, it is conceivable that the overall order parameter $\bar{\eta}$ is a selection factor that determines the nature of all possible radiation-induced patterns; this dependence does not appear in Fig. 1.

A. Structure factor

To describe nano-structures in the (PD) area ($\Delta_{min} < \Delta < \Delta_{max}$), a structure factor $S(k, t) = \langle|\hat{\eta}(\mathbf{k}, t)|^2\rangle$ (where $\langle.\rangle$ is a radial average) can be extracted from the numerical resolution of Eq. (3) obtained by fixing the first and third spatial derivatives of $\eta(\mathbf{x}, t)$ to zero at the boundaries. An example of this structure factor is plotted in Fig. 2 for an $Ag_{0.38}Cu_{0.62}$ alloy ($\bar{\eta} = 0$) irradiated at 440 K by 1 MeV Kr ions [values of a_j, κ, $\Gamma_{irr}(\phi)$, and $\Gamma_{th}(T, \phi)$ used in our 2D simulations can be found in Ref. 12]. The 2D steady-state pattern shown in the left-hand side of Fig. 2 was obtained by fixing the overall composition ($\overline{\psi} = 0$) and is in fair agreement with 2D patterns predicted by KMC simulations for the AgCu alloy[28] in the Bragg-William approximation, assessing our Phase Field approach.

B. The Swift-Hohenberg equation

At late-times [$t\Gamma_{th}(T, \phi) \gg 1$], the structure factor $S(k, t)$ is sharply peaked around $\mathbf{k_0}$ as clearly pointed in previous investigations.[11] As Eq. (3) is a Cahn-Hilliard like equation, the linear part of Eq. (3) acts as a low-pass filter at short times to dictate the characteristic wave vector of the patterning $\mathbf{k_0}$,[27] and it is not surprising that at late-times, S(k,t) exhibits a maximum at $\mathbf{k_0}$ minimizing the response function $D(k)$. Performing a second order Taylor expansion of $D(k)$ (such expansion is extensively used in the PFC approach based on the density functional theory[18,19,29]) at the vicinity of $\mathbf{k_0}$, the quadratic part of $\mathcal{L}'[\eta]$, thus reduces to $\int \frac{1}{2}\eta(\mathbf{r_2})\left[D(k_0) + \left(1 - \sqrt{\frac{\Delta_{min}}{\Delta}}\right)k_0^{-2}(\nabla^2 + k_0^2)^2\right]\eta(\mathbf{r_1})d\mathbf{r_1}d\mathbf{r_2}$, which is no more than the quadratic part of the Swift-Hohenberg functional extensively used to model pattern formation in non-equilibrium systems.[3]

Ground states of the SH functional are defined by periodic modulations of $\eta(\mathbf{r}, t)$ associated with a wave vector $\mathbf{k_0}$ and differ from the homogeneous ground states derived from the minimization of the Cahn-Hilliard equation.[27]

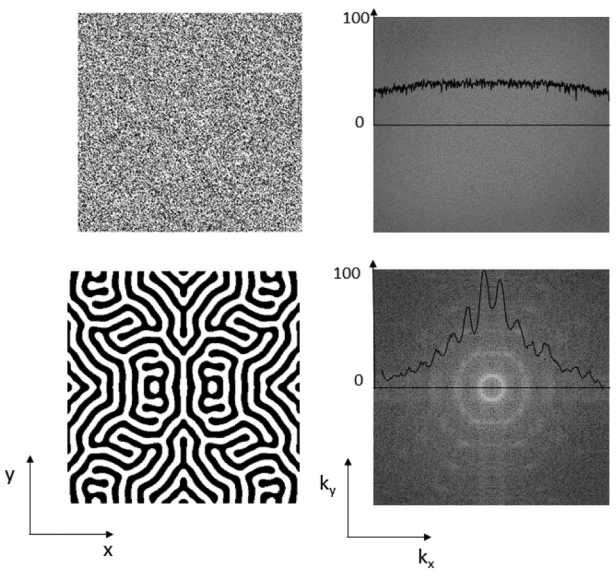

FIG. 2. 2D simulation of a random distribution of a $Ag_{0.38}Cu_{0.62}$ alloy, before (top) and after (bottom) irradiation with 1 MeV Kr ions at $\phi = 6 \times 10^{12}$ cm^{-2} s^{-1} and $T = 440$ K obtained from the numerical solution of Eq. (3) ($R = 3$ and $\Delta = 0.2$). Initial (up left-hand side) and final (down left-hand side) 2D micro-structures in real space and their corresponding Power Spectral Density (PSD) in the Fourier space (right-hand side) are plotted. In these simulations, A rich (black) [B rich (white)] domains are associated with positive (negative) η values (the 2D domain size is equal to 200 in reduced units). At late-time, the PSD is radially symmetric and peaks sharply around k_0 (intense white ring). Late-time structure factors $S(k, t)$, resulting from a circular average of the PSD for both initial (top) and final micro-structures (bottom), are plotted as a full line along the k_x component of the wave vector.

By the following relationships, $r'_i = k_0 r_i$, $\psi = \left(\eta + \frac{a_3}{a_4}\right)\left(1 - \sqrt{\frac{\Delta_{min}}{\Delta}}\right)^{-1/2}(k_0\alpha)^{-1}$, $\mathcal{L}'[\eta]$ reduces to the standard SH form[3,16,17]

$$\mathcal{L}_{SH}[\psi] = \int \frac{\psi(\mathbf{r}'_2)}{2}\left[-\epsilon(R, \Delta) + (1 + \nabla^2)^2\right]\psi(\mathbf{r}'_1)dr'_1dr'_2 + \int \frac{\psi(\mathbf{r}'_1)^4}{4}dr'_1, \quad (4)$$

where ψ is the reduced scalar order parameter field and $\mathcal{L}_{SH}$ is the reduced SH functional equal to $\frac{\mathcal{L}'[\eta]}{\left(1-\sqrt{\frac{\Delta_{min}}{\Delta}}\right)^{-2} k_0}$.

The term $\epsilon(R, \Delta) \propto D(k_0)$ is related to the minimum of the quadratic part of the Lyapunov functional $D(k)$, i.e., the Fourier transform of the effective interaction energy related to the global dynamics. This effective interaction takes into account not only pairwise interaction energies but also non local ballistic effects induced by irradiation. This energetic parameter thus contains all the physics associated with the formation of radiation-induced steady states. This reduced free energy term $\epsilon(R, \Delta) = \frac{2\sqrt{\Delta}(\sqrt{\Delta_{max}} - \sqrt{\Delta})}{(\sqrt{\Delta} - \sqrt{\Delta_{min}})^2}$ only depends on $R \propto R_p \propto \sqrt{\frac{\kappa}{a_4}}$ and $\Delta \propto \frac{\Gamma_{irr}(\phi)}{\Gamma_{th}(\phi, T)}\frac{\kappa}{a_4}$, which contains both information on ballistic effects and material properties. In this expression, $\epsilon(R, \Delta)$ contains all the information about the global dynamics.

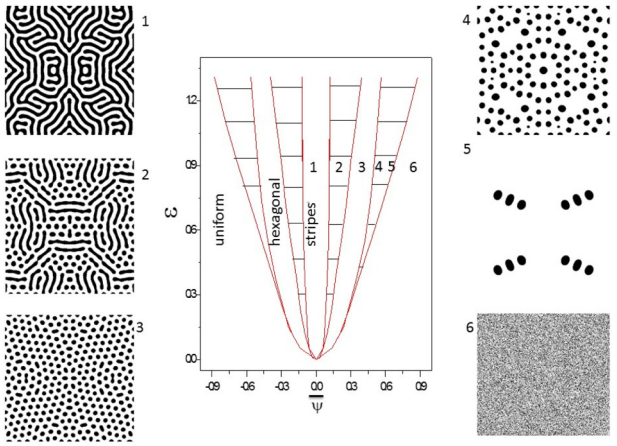

FIG. 3. Proposed generic 2D "Pseudophase diagram" in the (PD) area derived from the SH functional as function of the nominal composition, $\overline{\psi}$ and the $\epsilon(R, \Delta)$ parameter. The solid lines represent the limits between different micro-structures and the hatched area is associated with coexistent domains. This "pseudophase diagram" is in fair agreement with 2D simulated microstructures (graphs 1–6) resulting from the numerical resolution of Eq. (3) (from top-left to bottom-right, 1: $\overline{\psi} = 0$, 2: $\overline{\psi} = 0.2$, 3: $\overline{\psi} = 0.35$, 4: $\overline{\psi} = 0.5$, 5: $\overline{\psi} = 0.65$, 5: $\overline{\psi} = 0.7$ and $\epsilon = 0.85$).

IV. DYNAMICAL PHASE DIAGRAM

This approximation of the Lyapunov functional by a SH functional $\mathcal{L}_{SH}$ in the pattern domain is the keystone result of this study. Ground states of the SH functional are not only a function of $\epsilon(R, \delta)$ but also of the overall composition of the alloy $\bar{\psi}$ (in reduced units), which has been neglected in previous studies.[11,15] This implies that a more generic "pseudophase diagram" including the overall composition of the alloy can be drawn (Fig. 3) to extend previous studies.

A. Morphology of the nano-structure

2D ground states,[30,31] resulting from the minimization of $\mathcal{L}_{SH}$, can be analytically computed

- a uniform micro-structure with $\psi(\mathbf{r}) = \overline{\psi}$ (graph 6 in Fig. 3)
- a labyrinthine micro-structure (stripes) with compositional fluctuations, $\psi(\mathbf{r}) = \overline{\psi} + A_s\cos(\mathbf{kr})$ and wave vectors, $\mathbf{k} = k_0\begin{pmatrix}1\\0\end{pmatrix}$ and $\mathbf{k} = k_0\begin{pmatrix}0\\1\end{pmatrix}$ (graph 1 in Fig. 3). In the one mode approximation, [7] the amplitude of the modulation is equal to [30] $A_s = \frac{2}{3}\sqrt{3\epsilon(R, \Delta) - 9\overline{\psi}^2}$
- a honeycomb structure (hexagonal dots) with compositional fluctuations $\psi(\mathbf{r}) = \overline{\psi} + A_h\sum_{j=1}^{3} e^{i\mathbf{k}_j\cdot\mathbf{r}} + c.c.$ and wave

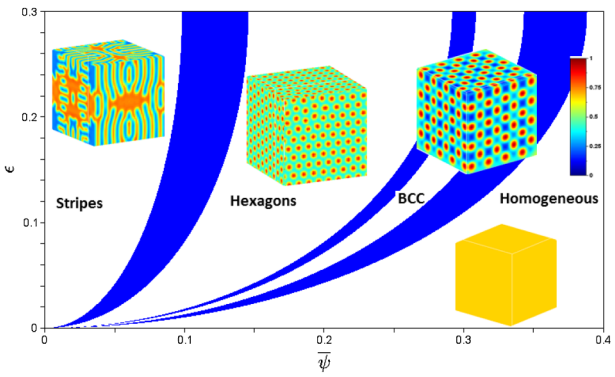

FIG. 4. Comparison between different 3D micro-structures extracted from direct simulations on the global dynamics and the theoretical phase diagram derived from the SH functional as function of the nominal composition, $\overline{\psi}$ and $\epsilon(R, \Delta)$. Co-existence domains are drawn in blue. All 3D numerical simulations were performed for $\epsilon = 0.25$ and at different $\bar{\psi}$ values: $\bar{\psi} = 0$ stripes, $\bar{\psi} = 0.25$ hexagons, $\bar{\psi} = 0.33$ BCC lattice of A-rich precipitates, and $\bar{\psi} = 0.4$ homogeneous phase (red: pure A phase, blue: pure B phase).

vectors, $\mathbf{k_1} = k_0\begin{pmatrix}1\\0\end{pmatrix}$, $\mathbf{k_2} = k_0\begin{pmatrix}-1/2\\\sqrt{3}/2\end{pmatrix}$, and $\mathbf{k_3} = k_0\begin{pmatrix}-1/2\\-\sqrt{3}/2\end{pmatrix}$ (graph 3 in Fig. 3). In the one mode approximation,[7] the amplitude of the modulation is equal to[30] $A_h = \frac{4}{5}\left[\overline{\psi} + \frac{\sqrt{15\epsilon(R,\Delta) - 36\overline{\psi}^2}}{3}\right]$.

These 2D ground states are in very good agreement with snapshots of late-time micro-structures extracted from our 2D numerical simulations (graphs in Fig. 3). Labyrinthine lamellar stripes forming at low $|\bar{\psi}|$ (snapshot 1 in Fig. 3) evolve to a honeycomb structure of spherical precipitates forming for intermediate $|\overline{\psi}|$ values (snapshot 2 in Fig. 3) and lead to a homogeneous solid solution forming at large $|\overline{\psi}|$ values (snapshot 3 in Fig. 3). Phase domains can co-exist (graphs 4, 5, and 6 in Fig. 3) as expected from the 2D theoretical phase diagram (full line in Fig. 3). Snapshots of 2D simulations prove that the ground states in the pattern domain (hatched area in Fig. 1) are not unique and cannot be modeled by a simple hyperbolic tangent profile leading the previous computations of the phase limits between the(SS) and the (SD) domains questionable.[15]

Extension of this analysis to three dimensions is straightforward. Figure 4 displays the theoretical phase diagram computed using the one-mode approximation for a 3D microstructure derived from the SH equation [Eq. (4)] and the 3D numerical resolution of Eq. (3). The diagram is computed minimizing the Lyapunov functional $\mathcal{L}_{SH}[\psi]$. For very low $\bar{\psi}$ values, the 3D micro-structure is made of different stripes. For small $\bar{\psi}$ values, hexagonal structures of A-rich precipitates appear as in 2D. Increasing $\bar{\psi}$, these precipitates form a body-centered cubic (BCC) structure that does not exist in the 2D dynamical phase diagram. For large $\bar{\psi}$ values, a homogeneous phase occurs. As it is the case for 2D simulations, all micro-structures predicted by the SH model have been observed by the numerical resolution of the global dynamics assessing the validity of our approach in 3D. Co-existence regions between these different pure domains can also be formed as plotted in Fig. 4. As pointed out by previous authors,[32] it must therefore be noticed that the one-mode approximation applied in this work is only valid in 3D for small ϵ values. For $\epsilon > 0.35$, face-centered cubic and hexagonal close packed A rich precipitates can form as a function of $\bar{\psi}$. As the free energy associated with these micro-structures is very small in comparison with the BCC phase, only 3D numerical resolution of Eq. (4) can provide the full dynamical phase diagram.[32]

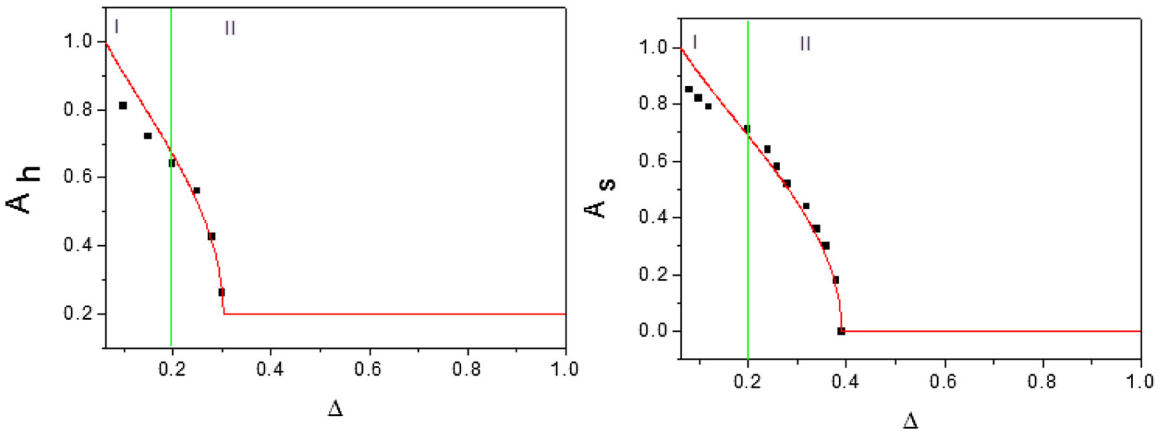

FIG. 5. Comparison of solubility limits A_s and A_h (full red line) calculated from the minimization of the 2D SH functional and extracted from 2D numerical simulations (black squares) for the honeycomb (left, $\overline{\psi} = 0.25$) and the labyrinthine (right, $\overline{\psi} = 0$) micro-structures for different Δ values ($R = 3$).

B. Induced solubility limits

Besides identification of different nano-structures, ground states of $\mathcal{L}_{SH}[\psi]$ also provide the solubility limits of precipitates in the pattern domain (A_S and A_h in 2D). These solubility limits are functions of $\overline{\psi}$. Such a dependence was systematically omitted in previous calculations of radiation-induced solubility limits.[15,33] Figure 5 displays variation of these solubility limits as a function of Δ (full red lines). The comparison between theoretical (full line) and calculated [from Eq. (3)] (black squares) solubility limits is in very good agreement in the vicinity of the (SS) domain for whichϵ tends to zero (region II in Fig. 5) and the one mode approximation holds.[16] This agreement does not hold in the vicinity of the (SD) domain for which ϵ tends to ∞ (region I in Fig. 5). This limitation can be easily overcome by introducing higher order mode expansions.[16]

V. CONCLUSION

Prediction and modeling of radiation-induced disordering is a long term goal in the advanced materials community. Our study proves that patterns produced by ion beam mixing in non-miscible alloys result from the existence of a Swift-Hohenberg functional $\mathcal{L}_{SH}$ and that the radiation-induced nano-structure in the pattern domain is not unique. All possible nano-structures, resulting from the minimization of the SH functional, can be drawn in a generic "dynamical phase diagram" highlighting the impact on the overall composition, up to now neglected.[13,15] Thus, this approach offers a novel quantitative method to design new classes of nano-materials by tuning not only the temperature and the flux of incident particles but also the overall composition of the alloy.

ACKNOWLEDGMENTS

This work was supported by the French initiative of basic research (CEA/RSTB) for the nuclear industry. G.L.M. thanks the support of the Australian Institute of Nuclear Science and Engineering (AINSE) and also funding from the SAAFE scholarship.

APPENDIX A: DIMENSIONLESS SYMMETRIC FREE ENERGY DENSITY

Within the Landau framework of phase transition, the free energy density associated with a decomposition is a first order transition and exhibits an odd term

$$f[\eta(\mathbf{r},t)] = \frac{a_2}{2}\eta(\mathbf{r},t)^2 + \frac{a_3}{3}\eta(\mathbf{r},t)^3 + \frac{a_4}{4}\eta(\mathbf{r},t)^4, \tag{A1}$$

where $\eta(\mathbf{r},t) = c(\mathbf{r},t) - c_0$. The negative a_3 term is associated with the asymmetry of the equilibrium phase diagram. Introducing two solubility limits given by the equilibrium phase diagram $\eta_\pm = -\frac{a_3}{3a_4} \pm \sqrt{\frac{1}{3}\left(\frac{a_3}{a_4}\right)^2 - \frac{a_2}{a_4}}$, the value of $\eta(\mathbf{r},t)$ varies from η_- to η_+. It is possible to rewrite this free energy density in a standard form

$$f[\eta'(\mathbf{r},t)] = \frac{3\lambda^2-1}{2}\eta'(\mathbf{r},t)^2 - \frac{\lambda}{3}\eta'(\mathbf{r},t)^3 + \frac{\eta'(\mathbf{r},t)^4}{4}, \tag{A2}$$

where $\alpha = \frac{\eta_+-\eta_-}{2}$, $\lambda = \frac{\eta_++\eta_-}{\eta_+-\eta_-}$, and $\eta'(\mathbf{r},t) = \frac{c(\mathbf{r},t)-c_0}{\alpha}$. $\eta'(\mathbf{r},t)$ varies from $\frac{2\eta_-}{\eta_+-\eta_-}$ to $\frac{2\eta_+}{\eta_+-\eta_-}$. Only for the case $a_3 = 0$, $\eta'(\mathbf{r},t)$ varies from -1 to 1. Introducing the reduced order parameter $\rho(\mathbf{r},t) = \eta'(\mathbf{r},t) - \lambda$, the free energy term can be expanded according to this new variable. In this rescaling, the three order terms vanish. The functional derivation of the free energy F implies that constant terms can be ignored in the expansion of the free energy density. Moreover, the conservative nature of the global dynamics, i.e., the Laplacian in Eq. (3), implies that linear terms proportional to $\rho(\mathbf{r},t)$ in $F[\rho]$ can also be ignored. The part of interest in the free energy density thus reduces to $\frac{\rho(\mathbf{r},t)^4}{4} - \frac{\rho(\mathbf{r},t)^2}{2}$, which is symmetric with respect to $\rho = \frac{c(\mathbf{r},t)-c_0+\frac{a_3}{3a_4}}{\alpha}$ leading to Eq. (4). In this last expression, $\psi(\mathbf{r},t) = \rho(\mathbf{r},t)k_0^{-1}\left(1-\sqrt{\frac{\Delta_{\min}}{\Delta}}\right)^{-\frac{1}{2}}$.

APPENDIX B: CALCULATION OF GROUND STATES IN THE ONE-MODE APPROXIMATION

The one-mode approximation of the concentration profile $\psi(\mathbf{r})$ associated with steady states is of the form

$$\psi(\mathbf{r}) = \bar{\psi} + A_i\psi_i(\mathbf{r}), \tag{B1}$$

where $\bar{\psi}$ is the mean value of $\psi(\mathbf{r})$, A_i is the amplitude of the concentration fluctuation, and $\psi_i(\mathbf{r})$ are the test functions obtained by summing with equal weights plane waves described by wave vectors characterizing the micro-structures (stripes, hexagonal network of bubbles, etc.). For various microstructures, the $\psi_i(\mathbf{r})$ are

For 2D micro-structures,

$$\psi_s(x,y) = \cos(kx), \tag{B2}$$

$$\psi_h(x,y) = \cos(kx)\cos\left(\frac{ky}{\sqrt{3}}\right) - \frac{1}{2}\cos\left(\frac{2ky}{\sqrt{3}}\right). \tag{B3}$$

For 3D micro-structures,

$$\psi_{bcc}(x,y,z) = \cos(kx)\cos(ky) + \cos(kx)\cos(kz) + \cos(ky)\cos(kz). \tag{B4}$$

The free energy given by Eq. (4) is then analytically calculated. This expression is thus minimized with respect to A and k to find the analytic approximation of the concentration profile. After computing the minimum of the free energies of all phases, co-existence domains were numerically calculated via the common tangent construction.

REFERENCES

[1]G. Nicolis and I. Prigogine, *Self Organization in Nonequilibrium Systems: From Dissipative Structure to Order Through Fluctuations* (Wiley, NY, 1977).
[2]M. Seul and D. Andelman, "Domain shapes and patterns: The phenomenology of modulated phases," Science **267**, 476 (1995).
[3]M. C. Cross and P. C. Hohenberg, "Pattern formation outside of equilibrium," Rev. Mod. Phys. **65**, 851–1112 (1993).
[4]M. Wang, R. Averback, P. Bellon, and S. Dillon, "Chemical mixing and self-organization of nb precipitates in cu during severe plastic deformation," Acta Mater. **62**, 276 (2014).
[5]A. Barbu, G. Martin, and A. Chamberod, "Low-flux radiation-induced precipitation," J. Appl. Phys. **51**, 126192 (1980).
[6]H. Bernas, J.-P. Attané, K.-H. Heinig, D. Halley, D. Ravelosona, A. Marty, P. Auric, C. Chappert, and Y. Samson, "Ordering intermetallic alloys by ion irradiation: A way to tailor magnetic media," Phys. Rev. Lett. **91**, 077203 (2003).
[7]N. Ghoniem and D. Walgraef, *Instabilities and Self Organization in Materials* (Oxford Science Publications, 2008), Vol. I.
[8]D. Simeone, J. Ribis, and L. Luneville, "Continuum approaches for modeling radiation-induced self-organization in materials: From the rate theory to the phase field approach," J. Mater. Res. **33**, 440–454 (2018).
[9]R. A. Enrique and P. Bellon, "Nonequilibrium fluctuations, effective temperature, and effective interactions driven by irradiation of alloys," Phys. Rev. B **70**, 224106 (2004).
[10]R. A. Enrique, K. Nordlund, R. S. Averback, and P. Bellon, "Simulations of dynamical stabilization of Ag-Cu nanocomposites by ion-beam processing," J. Appl. Phys. **93**(5), 2917 (2003).
[11]D. Simeone, G. Demange, and L. Luneville, "Disrupted coarsening in complex Cahn-Hilliard dynamics," Phys. Rev. E **88**, 032116 (2013).
[12]G. Demange, L. Luneville, V. Pontikis, and D. Simeone, "Prediction of irradiation induced microstructures using a multiscale method coupling atomistic and phase field modeling: Application to the AgCu model alloy," J. Appl. Phys. **121**, 125108–125122 (2017).
[13]L. Luneville, K. Mallick, V. Pontikis, and D. Simeone, "Patterning in systems driven by non local external forces," Phys. Rev. E **94**, 052126 (2016).
[14]R. A. Enrique and P. Bellon, "Self organized Cu-Ag nanocomposites synthesized by intermediate temperature ion-beam mixing," Appl. Phys. Lett. **78**(26), 4178 (2001).
[15]R. A. Enrique and P. Bellon, "Compositional patterning in systems driven by competing dynamics of different length scale," Phys. Rev. Lett. **84**(13), 2885–2888 (2000).
[16]M. Cross and H. Greenside, *Pattern Formation and Dynamics in Nonequilibrium Systems* (Cambridge University Press, Cambridge, 2009).
[17]K. Elder, M. Katakowski, M. Haataja, and M. Grant, "Modelling elasticity in crystal growth," Phys. Rev. Lett. **88**, 245701 (2002).
[18]Y. Jin and A. Katchaturyan, "Atomic density function theory and modelling of microstructure evolution at the atomic scale," J. Appl. Phys. **100**, 013519 (2006).
[19]A. Jaatinen and T. Ala-Nissila, "Atomic density function simulations of crystal growth kinetics of FCC crystal and BCC-FCC transition," J. Solid State Phenom. **172**, 1234 (2011).
[20]P. Subramanian and J. Perepezko, "The Ag-Cu system: A phase diagram evaluation," J. Phase Equilib. **14**, 62 (1993).
[21]A. G. Khatchaturyan, *Theory of Structural Transformation in Solids* (Wiley Interscience, 1983).
[22]P. Tolédano and V. Dmitriev, *Reconstructive Phase Transitions: In Crystals and Quasicrystals* (World Scientific, 1996).
[23]A. Gras-Marti and P. Sigmund, "Distortion of depth profiles during ion bombardment II. Mixing mechanisms," Nucl. Instrum. Methods B **180**(1), 211–219 (1981).
[24]D. Simeone and L. Luneville, "Concentration profile distortion under ion beam mixing: An example of levy flight," Phys. Rev. E **81**, 021115 (2010).
[25]G. Demange, E. Antoshchenkova, M. Hayoun, L. Luneville, and D. Simeone, "Simulating the ballistic effects of ion irradiation in the binary collision approximation: A first step toward the ion mixing framework," J. Nucl. Mater. **486**, 26 (2017).
[26]A. J. Bray, "Theory of phase-ordering kinetics," Adv. Phys. **43**, 357–459 (1994).
[27]A. J. Bray and C. L. Emmott, "Lifshitz-slyozov scaling for late-stage coarsening with an order-parameter-dependent mobility," Phys. Rev. B **52**(2), R685 (1995).
[28]R. Enrique and P. Bellon, "No equilibrium fluctuations, effective temperature and effective interactions driven by irradiation of alloys," Phys. Rev. B **70**, 224106 (2004).
[29]G. Demange, M. Chamaillard, H. Zapolsky, M. Lavrskyi, A. Vaugeois, L. Luneville, D. Simeone, and R. Patte, "Generalization of the fourier-spectral eyre scheme for the phase-field equations: application to self assembly dynamics in materials," Comput. Mater. Sci. **144**, 11 (2018).
[30]K. Elder and M. Grant, "Modelling elastic and plastic deformations in nonequilibrium processing using pfc," Phys. Rev. E **70**, 051605 (2004).
[31]U. Thiele, M. Archer, and M. Robbins, "Localized states in the conserved swift-hohenberg equation with cubic nonlinearity," Phys. Rev. E **87**, 042915–1–042915–19 (2013).
[32]A. Jaatinen and T. Ala-Nissila, "Extended phase diagram of the 3d phase field crystal model," J. Phys. Condens. Matter **22**, 205402 (2010).
[33]G. Martin, "Phase stability under irradiation: Ballistic effects," Phys. Rev. B **30**(3), 53 (1984).